International Journal of Pharmaceutics 597 (2021) 120303

Contents lists available at ScienceDirect

International Journal of Pharmaceutics

journal homepage: www.elsevier.com/locate/ijpharm

Fabrication of hollow microneedles using liquid crystal display (LCD) vat polymerization 3D printing technology for transdermal macromolecular delivery

Iakovos Xenikakis [a], Konstantinos Tsongas [b], Emmanouil K. Tzimtzimis [b], Constantinos K. Zacharis [c], Nikoleta Theodoroula [d], Eleni P. Kalogianni [e], Euterpi Demiri [f], Ioannis S. Vizirianakis [d,g], Dimitrios Tzetzis [b,*], Dimitrios G. Fatouros [a,*]

[a] School of Health, Faculty of Pharmacy, Division of Pharmaceutical Technology, Aristotle University of Thessaloniki, Thessaloniki 54124, Greece
[b] Digital Manufacturing and Materials Characterization Laboratory, School of Science and Technology, International Hellenic University, School of Science and Technology, 14km Thessaloniki - N. Moudania, Thermi GR57001, Greece
[c] Laboratory of Pharmaceutical Analysis, Department of Pharmaceutical Technology, School of Pharmacy, Aristotle University of Thessaloniki, GR-54124, Greece
[d] School of Health, Faculty of Pharmacy, Laboratory of Pharmacology, Aristotle University of Thessaloniki, Thessaloniki 54124, Greece
[e] Department of Food Science and Technology, International Hellenic University, Sindos Campus, 57400 Thessaloniki, Greece
[f] Department of Plastic Surgery, Medical School, Papageorgiou Hospital, Aristotle University of Thessaloniki, Thessaloniki, Greece
[g] FunPATH (Functional Proteomics and Systems Biology Research Group at AUTH) Research Group, KEDEK - Aristotle University of Thessaloniki, Balkan Center, GR-57001 Thessaloniki, Greece

ARTICLE INFO

Keywords:
Hollow Microneedle Device
Liquid Crystal Display
Skin synthetic membrane
Finite Element Analysis
Mechanical testing
Octreotide-acetate

ABSTRACT

The present study aimed to fabricate a hollow microneedle device consisting of an array and a reservoir by means of 3D printing technology for transdermal peptide delivery. Hollow microneedles (HMNs) were fabricated using a biocompatible resin material, while PLA filament was used for the reservoirs. The fabricated microdevice was characterized by means of optical microscopy, scanning electron microscopy (SEM), Fourier-transform infrared spectroscopy (FTIR), contact angle measurements and leakage inspection studies to ensure the passageway of liquid formulations. Mechanical failure and penetration tests were carried out and supported by Finite Element Analysis (FEA). The cytocompatibility of the microneedle arrays was assessed to human keratinocytes (HaCaT). Finally, the transport of the model peptide octreotide acetate across artificial membranes was assessed in Franz cells using the aforementioned HMN design.

1. Introduction

Transdermal drug delivery is an attractive route of administration due to the high surface offered (~2m^2) (Gallo, 2017). However, the presence of *stratum corneum* (SC), which is the outermost skin layer, renders skin impermeable to the vast majority of solutes (Guy, 1996; Touitou, 2002). To overcome this biological barrier, several physical and chemicals methods have been proposed such as iontophoresis (Karpiński, 2018), sonophoresis (Nguyen and Banga, 2018), microneedle arrays (Larrañeta et al., 2016) and penetration enhancers (Calatayud-Pascual et al., 2018).

Microneedles (MN) are miniature devices (maximum length 1000 μm), capable of perforating painlessly SC and releasing their active content in the skin layers beneath (Ingrole and Gill, 2019). One of their major advantages, is their potential to replace the fear inducing syringe-based administration (Prausnitz, 2017). This advantage would alleviate patients whose medication is exclusively in injection form *e.g.* diabetics. Such medications include drugs of peptide nature, which are susceptible to degradation in gastrointestinal tract. Previously, hollow microneedles (HMN) have been used for insulin delivery (Gupta et al., 2009) and vaccines (Waghule et al., 2019). Interestingly, insulin demonstrated more efficient absorption and faster onset of pharmacological effect compared to subcutaneous injection, while vaccination was achieved at lower doses compared to intramuscular administration. Anticancer vaccination was also achieved modifying immune response with very low volumes of a liposomal peptide (van der Maaden et al., 2018). In the

* Corresponding authors.
E-mail addresses: d.tzetzis@ihu.edu.gr (D. Tzetzis), dfatouro@pharm.auth.gr (D.G. Fatouros).

https://doi.org/10.1016/j.ijpharm.2021.120303
Received 20 November 2020; Received in revised form 17 January 2021; Accepted 19 January 2021
Available online 2 February 2021
0378-5173/© 2021 Elsevier B.V. All rights reserved.

current study, octreotide acetate was used as a model peptide and was delivered through HMNs across artificial membranes. Octreotide acetate is a somatostatin analog used for the treatment of gigantism, acromegaly and thyrotropinoma (Gomes-Porras et al., 2020) and has been previously administered *in vivo* using electric current (Lau et al., 1994).

Previously, HMNs have been developed by means of microelectromechanical systems (MEMS) techniques (Kim et al., 2012). These approaches include laser micromachining (Davis et al., 2005), deep reactive ion etching of silicon (Roxhed et al., 2007), an integrated lithographic molding technique (Luttge et al., 2007), deep X-ray photolithography (Pérennès et al., 2006), and wet chemical etching and microfabrication (Ma et al., 2006). Finally a different approach suggest fabrication of master structures as a first step and then casting of a material suitable for microneedle formation (indirect fabrication) (Kim et al., 2012).

More recently, additive manufacturing (AM) has emerged as a promising alternative to the aforementioned multistep processes. AM offers the possibility to design the desired geometries of MNs using a computer aided design (CAD) software and materialize one-step free-mold fabrication through a 3D printer machine. Designs can be saved and modified, offering convenience and flexibility. This, in combination with the simple equipment required for such a process, have raised scientific interest on MN fabrication *via* AM methods (Jamroz et al., 2017). Two photon polymerization (TPP) was first employed for the fabrication of HMNs (Doraiswamy et al., 2006). The same approach was used by Gittard *et al.* for in plane and out of plane HMN fabrication. TPP has been further reported for the manufacture of ceramic and acrylate based HMNs (Gittard et al., 2011, 2010; Ovsianikov et al., 2007). In another study a digital micromirror device based on stereolithography method enabled the HMN fabrication with the perspective of utilizing them as electrochemical transducers (Miller et al., 2011). The past few years stereolithography (SLA) was also introduced for microfluidic enabled MN array production (Farias et al., 2018; Yeung et al., 2019). A single compartment of HMN and drug reservoir by means of TPP method was recently reported by Moussi *et al.* whereas in a different approach HMN were fabricated by means Selective Laser micro-Melting is referred (Gieseke et al., 2012; Moussi et al., 2020). Yet, vat polymerization methods include additional methods apart from SLA and TPP.

Digital Light Processing (DLP) and Liquid Crystal display (LCD) are two methods which are based on UV mediated resin solidification and have not been investigated for HMN fabrication. Among all these methods, LCD vat polymerization provides an inexpensive and satisfying resolution (below 50 μm) 2 K LED screen, which enables the fabrication of microstructures with complex architectures (Mohamed et al., 2019). Reducing manufacturing costs, 3D printed objects would be more accessible to developing countries and low-income individuals.

In the current study, HMNs were fabricated using LCD, which offers the accuracy required for microstructures like HMNs. HMNs were evaluated for their flow capability whereas reservoirs manufactured by Fused Deposition Modeling (FDM) assembled with HMN arrays and checked for any leakage. Penetration tests were performed on both human skin and synthetic membranes and compression failure tests of the HMNs were carried out using a mechanical testing machine, in order to estimate insertion force and safety factor, respectively. In parallel FEA simulations complemented the experimental data. The cytocompatibility of 3D-printed HMNs was evaluated in HaCaT cell lines. Permeability studies of octreotide-acetate across synthetic membranes, were conducted using with Franz diffusion cells. The samples were analyzed with a high-pressure liquid chromatographic (HPLC) method developed and validated in-house for the intended purpose. Finally, octreotide stability was evaluated under the tested conditions.

2. Materials and methods

2.1. Materials

Nextdent Ortho Rigid resin (Nextdent B.V., Netherlands) was purchased from Nextdent local supplier (Dentalcom Papazoglou S.A., Greece). PLA filament was obtained from 3D Hubs (Netherlands). Isopropyl alcohol (≥98%, GC), methylene blue, absolute ethanol (≥98%, GC), Pluronic F-127, 40% polyacrylamide solution (acrylamide: bisacrylamide 37.5:1), ammonium persulfate (APS), N,N,N',N'-tetramethylenediamine (TEMED), fluorescein isothiocyanate–dextran (FITC-dextran) (MW 4000 Da), calcein, Strat-M® membranes, disodium hydrogen phosphate dodecahydrate ($Na_2HPO_4{\cdot}12H_2O$), potassium dihydrogen phosphate (KH_2PO_4), sodium chloride (NaCl), potassium chloride (KCl), trifluoroacetic acid (>99%), Human adult low calcium cell lines (HaCaT), sterile phosphate buffer saline (PBS) powder, Dulbecco's Modified Eagle Medium (DMEM), Glutamax, Fetal Bovine Serum (FBS), 1% of 10 mg/mL Streptomycin and 10.000U/mL Penicillin, trypsin and trypan blue were purchased from Sigma Aldrich (St Louis MO, USA). Acetonitrile and water (HPLC grade) were obtained by VWR chemicals (Vienna, Austria). Octreotide acetate was kindly donated from Pharmathen S.A. (Greece).

2.2. Microneedle design and fabrication

HMN arrays (3 × 3) were designed in Solidworks CAD software (Dassault Systèmes, SolidWorks Corporation, Waltham, MA, USA) and exported as .STL file. HMNs were designed with different heights around 1000 μm, different shapes and tip diameters and several hole formations, in an attempt to investigate the optimal print setup. The interspacing of MNs was set constant at 3000 μm (center to center distance) and the whole patch was a 15 × 15 mm square. 3D printing fabrication was performed using Phrozen Shuffle 2018 utilizing LCD method with the curring process applied in each layer avoiding post fabrication treatment. NextDent Ortho Rigid, a biocompatible Class IIa resin, was used as the printing material. Designs from Solidworks were further processed with ChiTuBox 64 slicer setting the printing angle, the curing time and the printing resolution. Lifting speed was at 400 μm/s whereas different printing angles and resolutions were tested. The fabrication proccess of the mcironeedles had an average duration of *ca.* 3 h and 18 min.

At the end of the process HMN arrays were rinsed with isopropyl alcohol for three min in a ultrasonic processor (Hielscher UP200s, Teltow, Germany) and subsquently with the same solvent for another 2 min. The amplitude of the processor was set at 35% while the pulse was around 40–45%. Finally, HMNs were dried in an air-circulated oven (Binder FD115, Tuttlinger, Germany) for 20 min at around 25–27 °C and supports were carefully removed.

PLA reservoir was designed in Solidworks and fabricated with FDM BCN3D Sigma R17 3D (BCN3D, Barcelona, Spain) printer. Ultimaker Cura (Ultimaker, Utrecht, Netherlands) was used as slicing Software. The printing resolution was 100 μm, with 20% of grid infill pattern, whereas the extruder's and the heated bed's temperatures were 205 °C and 65 °C, respectively.

2.3. Microscopy studies of the 3D printed hollow microneedles

HMNs were visualized and their dimensions were measured using digital optical microscope Dino-Lite AB7013MZE (AnMo Electronics, Hsinchu, Taiwan) and software DinoLite 2.0. The morphology of HMNs was examined using SEM (Phenom ProX, ThermoFischer, USA). HMNs were mounted on a steel stub with double sided adhesive carbon tape and visualized under vacuum.

2.4. Microfluidic characterization

2.4.1. Methylene blue staining

HMNs were assessed for their flow ability initially by instilling 1 mg/mL of methylene blue of aqueous or isopropyl alcohol solutions in the microchannels (*ca.* 50 μL/microchannel). Beneath microneedle tips, filter paper was placed and checked for stains at the end of the procedure.

2.4.2. Surfactant addition

Due to the hydrophopic nature of the resin the microneedles were coated with aqueous solutions containing Pluronic F-127 at a final concentration of 1% w/v and 5% w/v respectively. Briefly, HMNs were placed in falcon tubes and covered with 10 mL of the surfactant solution. Subsequently, falcons were placed in ultrasound bath for 1 min to degas the interior of microchannels and left in room temperature for 30 min. Subsequently the HMNs were collected and placed for 10 min in the oven at 50 °C. The whole procedure was repeated four times. Upon completion of the coating procedure methylene blue staining studies were repeated to the modified microneedles.

2.4.3. FTIR spectroscopy studies

The coating of the microneedles was further assessed by means of FTIR spectroscopy. For this reason, spectra of 3D printed films of $1 \times 1 \times 0.3$ cm were recorded with a ATR-FTIR Prestige-21, Shimadzu in the range of 600–4000 cm^{-1}. Non-coated films served as controls.

2.4.4. Contact angle measurements

Spectroscopic data were complemented with contact angle goniometry studies. Contact angles of ultrapure water (resistivity 18 mΩ.cm at 25°C) with coated and non-coated polymerized resin material were determined in order to evaluate potential changes of surface properties after Pluronic F-127 coating. To carry out contact angle measurements twelve films from the resin with dimensions 2 cm × 2 cm × 0.5 cm were fabricated. Not treated films (n = 3) were serving as controls whereas the rest were coated with 1 w/v % (n = 3) and 5% w/v Pluronic F-127 (n = 6). Form the last group three films were further rinsed with 1 mL ultrapure water (Milli Q). The contact angles were measured by CAM200 (KSV) using the drop shape method. Measurements were taken at 25°C. Several ultrapure water microdroplets were formed at different positions of each 3D-printed film to assure homogeneous properties within the films. In addition, measurements were taken at all available 3D-printed films. Drop shape analysis and contact angle determination were performed by making use of the One-Attension software (version 1.8 Biolin Scientific).

2.4.5. Gel diffusion studies of model dyes

The diffusion of aqueous solutions of model dyes through the HMNs were monitored in gels composed of polyacrylamide (Schramm-Baxter et al., 2004). Briefly, polyacrylamide gel (20% w/w) was prepared by first adding 7 mL deionized water in an equal volume of 40% polyacrylamide solution (acrylamide: bis-acrylamide 37.5: 1). Subsequently, 140 μL 10% ammonium persulfate (APS) and 28 μL N,N,N',N'-tetramethylenediamine (TEMED) were added to the above diluted acrylamide solution (Schramm-Baxter et al., 2004) in cylindrical containers. Four gels were produced and microneedles were placed on their surface with tips being in contact. Aqueous solutions of FITC dextran (MW 4000) 0.2 mM and calcein 1 mM were prepared and 50 μL were instilled into each bottom channel of microneedle arrays. For each dye two gels were used. At specific time intervals (1 h, 3 h and 24 h), pictures were taken and dye diffusion in the gels was recorded.

2.4.6. Leakage inspection

HMN devices (HMNs assembled with reservoirs) were connected with a multi-channel peristaltic pump (205CA). Deionized water was pumped and pushed towards HMN devices, which were previously fastened in a grasp. During pumping, the rectangular perimeter interface between HMN patches and reservoir was inspected for possible leakages. Flow rate was set at 0.5 mL/min. Flexible tubing from platinum cured silicon material with 5 mm diameter was used for liquid transport.

2.5. Mechanical characterization and penetration tests

For both penetration and mechanical failure tests, HMN arrays were first examined with optical and scanning electron microscopy and compressed in a tensile test machine (M500-50AT Testometric Company, Rochdale, UK) with a 500 N load cell. HMNs were mounted on a steel rod, using double sided adhesive carbon tape and the rod was descending with a rate of 0.5 mm/min, mimicking a potential axial load an array of HMNs may experience during application.

The mechanical failure process was conducted with maximum compression forces up to 400 N, which are considered much higher than those applied during actual skin penetration. This procedure was repeated with at least three different HMNs arrays. At the end of the experiment, HMN arrays were inspected by means of scanning electron microscopy to detect any alterations caused by the compression forces.

Penetration tests were carried out by using skin samples. Skin was obtained from female donor (50 years old) who had been subjected to cosmetic surgery operation. Skin was immediately transferred to laboratory, and after being pinned on Styrofoam, fatty tissue was removed using scalpels. Subsequently, skin was placed (dermis side down) on a 500 μm thick dental wax and the whole on a wooden substrate (Olatunji et al., 2013) and placed on the bottom platen of the tensile machine.

Penetration tests were performed using the same rod descending rate with failure tests (0.5 mm/min). The penetration experiments were carried out applying forces up to 5 N for 1 min. When the desired load was exerted, the experiment was stopped and 50 μL methylene blue solution (1 mg/mL) were added to stain selectively the perforation sites (van der Maaden et al., 2014). The excess quantity of dye was wiped with tissue paper 10 min later and captures were taken.

Penetration tests were also conducted using synthetic membranes Strat-M® (Sigma Aldrich). The same procedure was followed by replacing skin samples with synthetic membranes. At the end, membranes were inspected using an optical microscope. Both skin and membrane penetration experiments were carried out in duplicate.

2.6. Cytocompatibility assessment of 3D-printed microneedles

HaCaT cells -attached type cells- were isolated by incubating HaCaT cell cultures with trypsin for 5 min (5% CO_2, 37ºC) which was neutralized with culture medium DMEM and centrifugated at 1200 rpm. The supernatant was discarded and the cell precipitate was mixed with DMEM containing 1% Glutamax, 10% FBS and 1% PS and a new cell suspension was formed. The number of cells was estimated by optical microscopy (56.7 × 105 264 cells/mL) and with proper dilutions were placed in 1 mL wells to achieve a concentration of 105 265 cells/mL . The well plate was left for 24 h the cells were attached to the wells and the next day culture medium was removed.

The *in vitro* cytotoxicity effects of LCD 3D printed HMNs in HaCaT cells was assessed by immersing three cubes of 1 cm^3 in 2.5 mL sterile PBS. At predetermined time points (2 h, 24 h and 48 h), 300 μL of PBS extract was removed and splitted into two parts: 100 μL and 200 μL. Cells counted with an optical microscope and were found to be

56.7 × 105 264 cells/mL, The samples were cultured in a 96 well plate containing 10^5 cells/mL. DMEM medium containing 1% Glutamax and supplemented by 10% FBS and 1% penicillin–streptomycin (PS) solution, and the PBS extracts, in a total volume of 1 mL. As controls were considered the following samples: medium without PBS and the other two contained 100 μL and 200 μL sterile PBS. Once new culture medium, controls and cube extracts were added in the wells, the plate was incubated for 48 h. Upon incubation, cells were detached using trypsin and culture medium and counted with the microscope and the

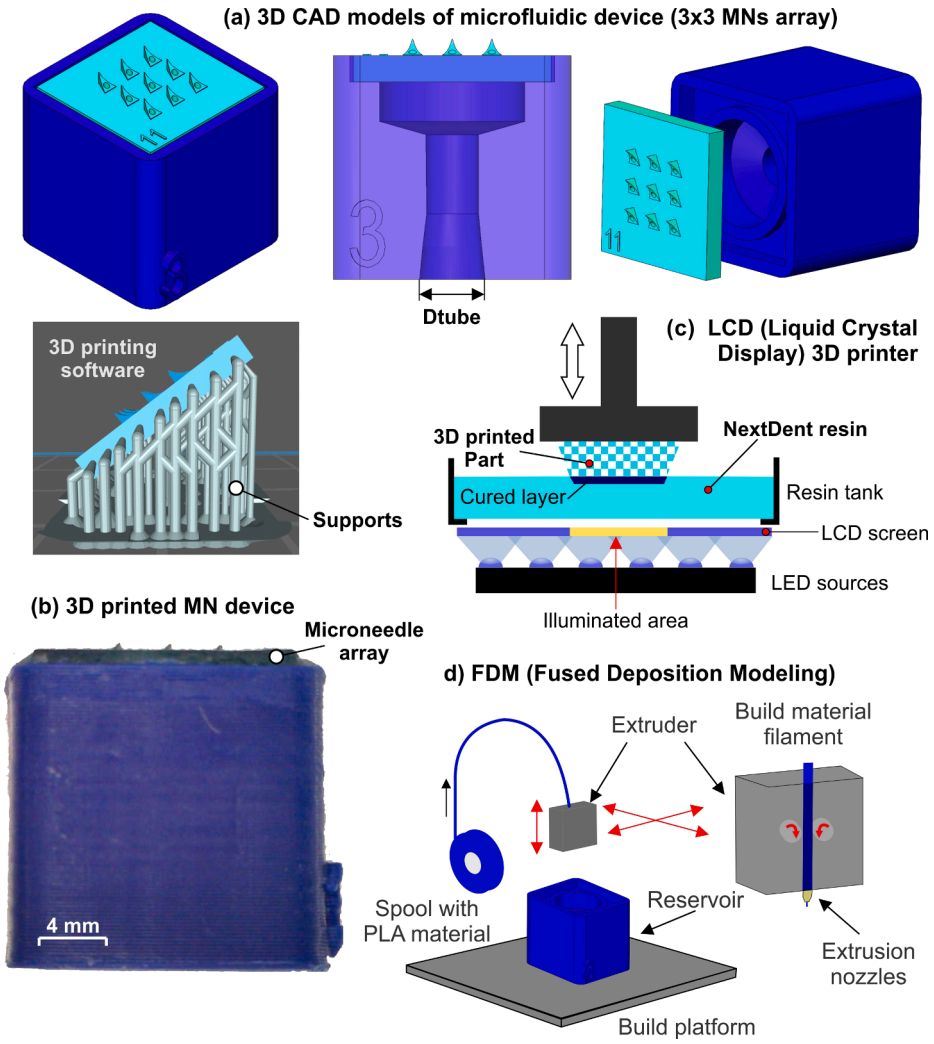

Fig. 1. 3D printing process of HMN devices (a) 3D CAD model of a representative HMN 3x3 array along with .STL model with supports in 3D printing platform, (b) 3D printed microneedle arrays fitted in a reservoir adapter suitable for drug administration, (c) Schematic representation of the LCD 3D printer for the fabrication of the HMN arrays and (d) Schematic representation of an FDM 3D printed for the fabrication of the reservoirs.

cell growth was assessed.

Furthermore, an aliquot of cells was mixed with 15 μL trypan blue and dead cells (cells stained blue) were counted with the microscope, assessing thus the percentage of cell death. Additionally, the same procedure was followed to determine the direct effect of commercial resin Nextdent Ortho Rigid on HaCaT cell growth. For this reason, 4 μL and 8 μL of the resin were incubated in the wells for 72 h.

2.7. Diffusion experiments

2.7.1. In vitro permeation study

Permeation study was carried out using vertical Franz diffusion cells and Strat-M® synthetic membranes. Strat-M® membranes were placed on dental wax (500 μm thickness) and both of them were pinned on a wooden substrate. HMN devices, were manually pressed on membranes for at least 30 s, performing periodically soothe vibrating moves. Next, membranes and HMN devices were transferred between donor and receptor of Franz cells. Receptor was previously filled with phosphate buffer saline pH 7.4 (PBS). Franz cells were kept in body temperature (37 °C) by circulating deionized water, preheated with thermostatic bath. Stirring was applied at 200 rpm. PBS was made dissolving 3.63g $Na_2HPO_4 \cdot 12H_2O$, 0.24g KH_2PO_4, 8g NaCl and 0.2g KCl in 1L deionized water.

Subsequently, the peptide solution (0.5 mg/mL) was pumped at a rate of 0.5 mL/min through HMN devices using the previously described set up. After infusion ended, pump was disconnected from reservoirs and donors were covered with parafilm to avoid evaporation. At predetermined time intervals (1 h, 2 h), samples of 1 mL were collected in glass vials for HPLC analysis and replaced with 1 mL of prewarmed PBS solution. The permeability studies were carried out in triplicate.

2.7.2. Octreotide stability studies

An aliquot of 5 mL of 0.5 mg/mL octreotide aqueous solution was prepared and kept at a constant temperature of 37 °C for 2 h. At specific time intervals (1 h, 2 h) an aliquot of 0.5 mL of the solution was sampled and transferred to HPLC vials. HPLC analysis was used to determine the amount of octreotide in each sample and the corresponding chromatographs were taken. Results were used to evaluate the stability of octreotide as a function of time at the certain temperature.

2.7.3. Octreotide acetate-Pluronic F-127 interactions

3D printed films of 1 cm^2 were placed between side by side Franz cell compartments using dental wax. Franz cells were filled with 0.5 mg/mL of octreotide acetate solution. Peptide solution was in contact with the film. At time intervals of 2, 5, 10 and 20 min, aliquots of 1 mL were taken, replaced with 1 mL of PBS solution and peptide quantification was performed by HPLC.

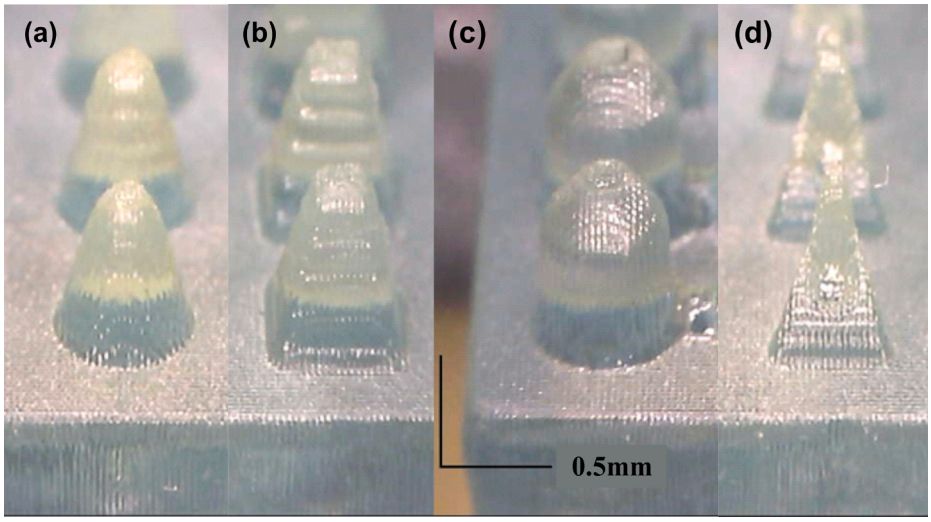

Fig. 2. Different geometries of HMNs: (a) cone, (b) square pyramid, (c) screw and (d) triangular pyramid.

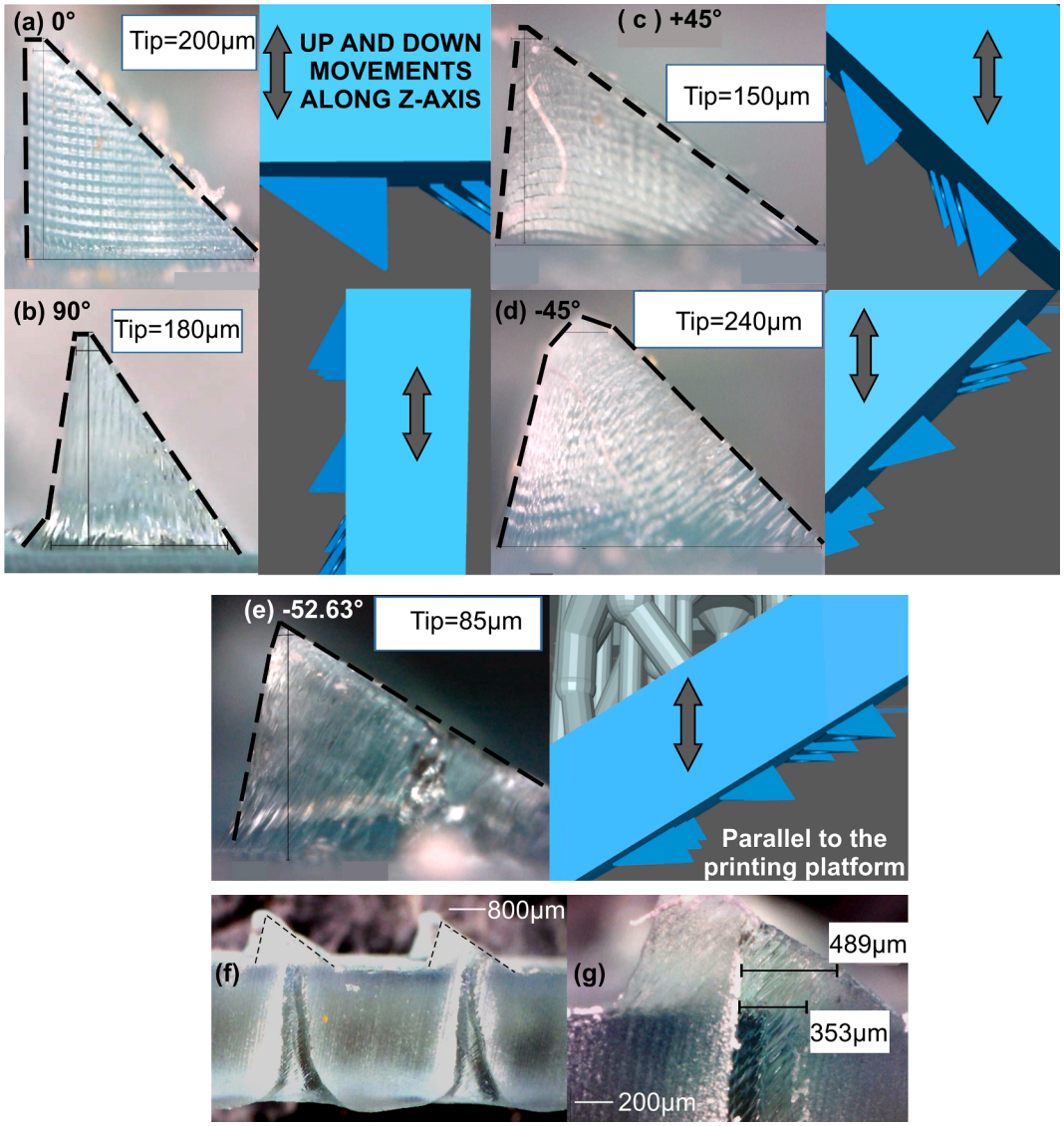

Fig. 3. Morphology characterization of the HMN formation and tip diameter (next to HMN optical images, the corresponding schematic is placed as derived from the ChiTuBox slicer) for each printing angle; (a) 0°, (b) 90°, (c) + 45°, (d) −45°, (e) −52.63°. The formation of the microchannels is shown in (f) and a higher magnification of the hole formation is illustrated in (g).

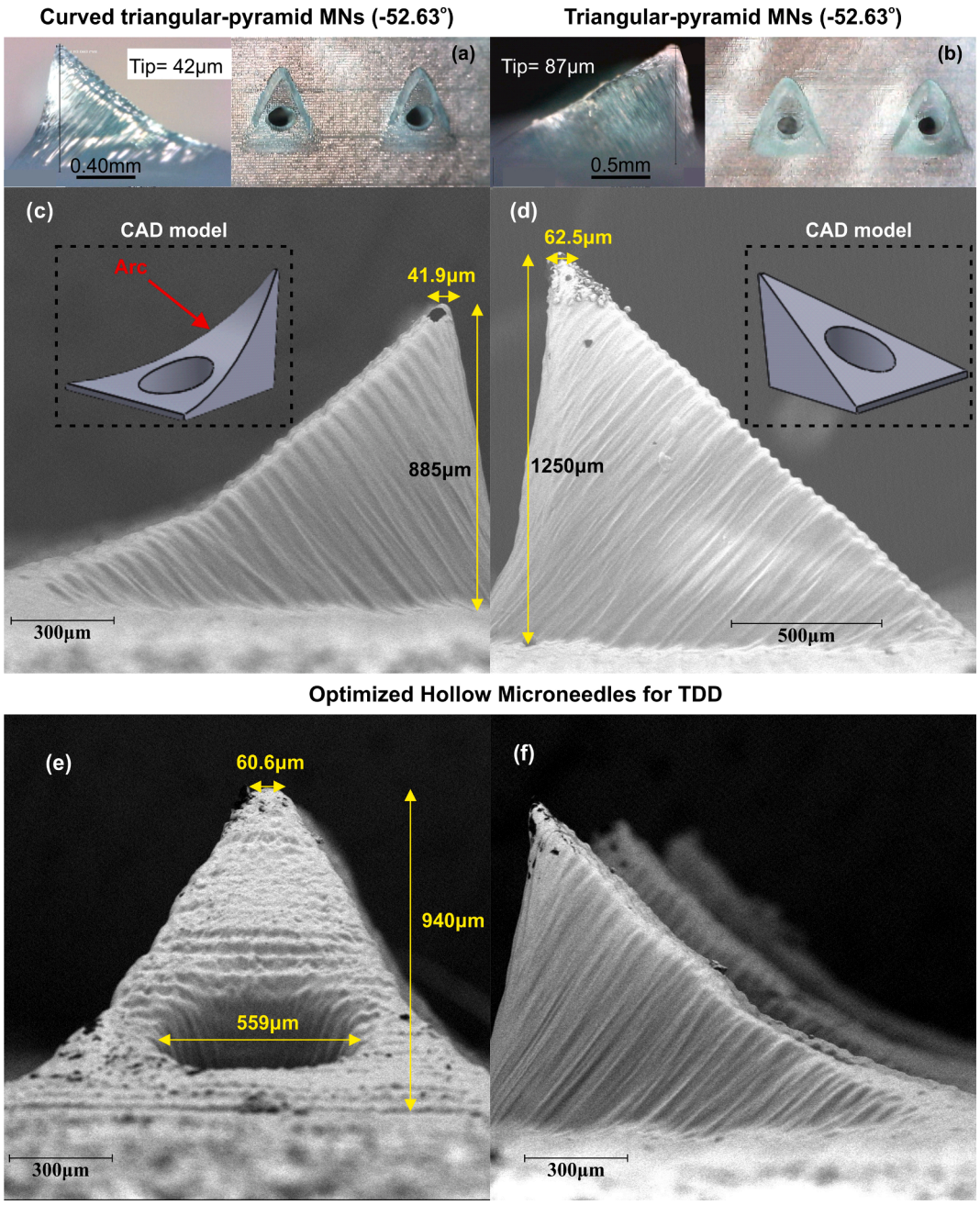

Fig. 4. Optical microscopy and SEM micrographs of optimized curved HMNs (a), (c), (e), (f) compared with the initial configuration of triangular-pyramid HMNs (b), (d).

2.8. HPLC analysis

Determination of octreotide-acetate was performed using an HPLC method developed and validated in-house for the intended purpose. All experiments were conducted using a Shimadzu HPLC system (Kyoto, Japan) consisting of two LC-20AD isocratic high-pressure pumps, a SIL-20C HT thermostated autosampler, a CTO-20AC thermostated column compartment and a SPD-M20A PDA detector. The control of the instrument and the data handling were carried out *via* the Lab Solutions software (version 5.42 SP3). Separations were performed on an analytical column Nucleodur C_{18} (125 × 4.6 mm, 5 μm) (Machery-Nagel, Germany) thermostated at 30 °C. The analyte was eluted using a binary gradient elution program including water (A) and acetonitrile (B) both acidified with trifluoracetic acid (0.1% v/v). The initial ratio was 5% v/v of B and then was linearly increased to 50% in 6 min. The next 1 min ratio was kept constant, then changed to the initial ratio (at 8 min) and finally stated until 15 min to maintain a stable and reproducible separation. The flow rate was set at 1.3 mL/min while the injection volume was 50 μL in all cases. The analyte was monitored spectrophotometrically at 210 nm. The processed samples were kept at 10 °C in the sampler tray and between injections the autosampler was washed with 50/50% v/v water/methanol to remove any sample residues. Under these conditions a sharp peak of octreotide was obtained at 7.6 min with number of theoretical plates higher than 60000. Seven calibration solutions were prepared in water to obtain a calibration curve. The calibration curve was linear in the studied range of 0.5–50 μg/mL with $R^2 = 0.9984$. The lower limit of quantitation was found to be 0.5 μg/mL and the % RSD of three replicate injections of standard solution was<1.0%.

2.9. Statistical analysis

The results for the transport studies and cell viability studies are presented as mean ± standard deviation of three experiments. Statistical differences were tested using unpaired Student *t*-test ($p < 0.05$).

3. Results and discussion

3.1. Optimization of hollow microneedle devices and 3D printing parameters

HMNs were designed with different shapes and heights in an attmept to define the optimal printing parameters. The assembly in SOLIDWORKS CAD software is demonstrated in Fig. 1(a). HMN patch dimensions were set constant at 15 × 15 mm whereas reservoir's height was set at 17 mm. The upper internal square perimeter was 3D-printed with slightly greater dimensions (15.5 × 15.5 mm) allowing HMN patches to fit in. At the bottom side, the reservoir had an aperture allowing tube connection, as shown in Fig. 1(a). This configuration enables liquids to flow *via* tubing reaching the bottom HMN channels. The inner space of reservoir had a funnel shape which inscribes all bottom microchannels. The assembly of the 3D-printed HMNs with the reservoir is depicted in Fig. 1(b). The final dimensions of the device were 18 × 18 × 17 mm (length × width × height). As illustrated in Fig. 1(c) and (d), an LCD and an FDM 3D printer were utilized to fabricate HMN arrays and reservoirs, respectively.

Resin used in LCD printings (Ortho Rigid, Nextdent) is a Class IIa biocompatible material according to European framework for medical devices, and thus 3D-printed material is appropriate for transdermal medical use, whereas the use of PLA as printing material ensures the biocompatibility of the reservoirs. FDM printed PLA (biocompatible) reservoir chambers were proved to provide a very efficient and appropriate way to fit with the removable microneedle arrays, offering a very fast and inexpensive solution.

The preliminary attempt to manufacture HMNs included different geometries, are shown in Fig. 2 where cone (Fig. 2(a)), square pyramid (Fig. 2(b)), screw (Fig. 2(c)) and triangular pyramid (Fig. 2(d)) were manufactured as precursor of the optimal HMNs. The triangular pyramid configuration was considered the most promising candidate providing sufficient printing repeatability and constant trend to yield sharper tips. Additionally, due to the fact that the hole is not located directly on the tip but on a side microneedle wall, liquid flow will encounter minor resistance during administration (Martanto et al., 2006). Therefore, a decision was made to continue our study with HMNs designed and 3D printed with a triangular-pyramid geometry and a triangular shaped tip.

The optimal 3D printing angle was also investigated. Different 3D printing angles were previously examined, namely 0°, +45°, −45° and 90°, as portrayed in Fig. 3. The printing angle of −45° gave the largest tip, but simultaneously it was the only one which resulted in the formation HMNs. Schematics of the HMNs were drawn (Fig. 3) on the printing platform for each case in ChiTuBox 3D printing slicer software. Subsequently, the printing process was simulated focusing on the up and down movements along the Z-axis. The resin flow appeared to influence the quality features of HMNs and their channel formation. It can be postulated that during printing movements along Z-axis, non-polymerized resin material is forced to flow on HMN surfaces that have already been produced. At 0°, +45° and 90°, resin flow is favored towards microchannel location. Due to resin aggregation and the upcoming polymerization cycle, microchannel formation is blocked. At −45° resin has minor trend to be driven inside the microchannel, probably because of the fact that HMNs' inclined plane is closer to a vertical position in relation to Z-axis, as shown in Fig. 3(d). This resulted in successful microchannel formation (100%).

Regarding the tip formation, at 0°, +45° and 90° resin excess material is partially impeded to reach the tip because it fills HMN channels. Hence, the amount of resin that finally reaches HMN tips is lower than the corresponding at −45°. This can explain the formation of larger tips at −45°.

Next, the optimal 3D printing parameters for obtaining simultaneously sharp tips and HMNs were investigated. Considering that sharp tips resulted after resin flow obstruction, an attempt was made to hinder resin flow at −45°, at least on one surface. For that reason, printing angle was changed at −52.63° with the aim of making the inclined surface of HMNs parallel to the printing platform (Fig. 3(e)). In this manner, resin flow on this surface is considered zero and at the same time HMN channels are fully protected. When a −52.63° printing angle was applied, sharp tipped HMNs were successfully fabricated, with a mean tip diameter of 85 μm. Previous HMN configurations have returned actual tip diameters of 200 μm, 180 μm, 150 μm and 240 μm for 0°, 90°, +45° and −45° respectively.

Considering the interaction of HMNs with skin or membrane material, the HMN tip should be sharp enough with a diameter close to 50 μm in order to successfully penetrate the first layer (Xenikakis et al., 2019; Yeung et al., 2019). HMNs were redesigned and 3D printed again, as portrayed in Fig. 4(a)–(d). The curved configuration (Fig. 4(a), (c)) provided the most promising HMNs, in terms of sharpness. The concept of moving to curved HMNs, was that the initial triangular-pyramid HMNs were too coarse at the tip region (estimated to be>0.01 mm^2) and this would impede insertion. Moreover, the triangular-pyramid

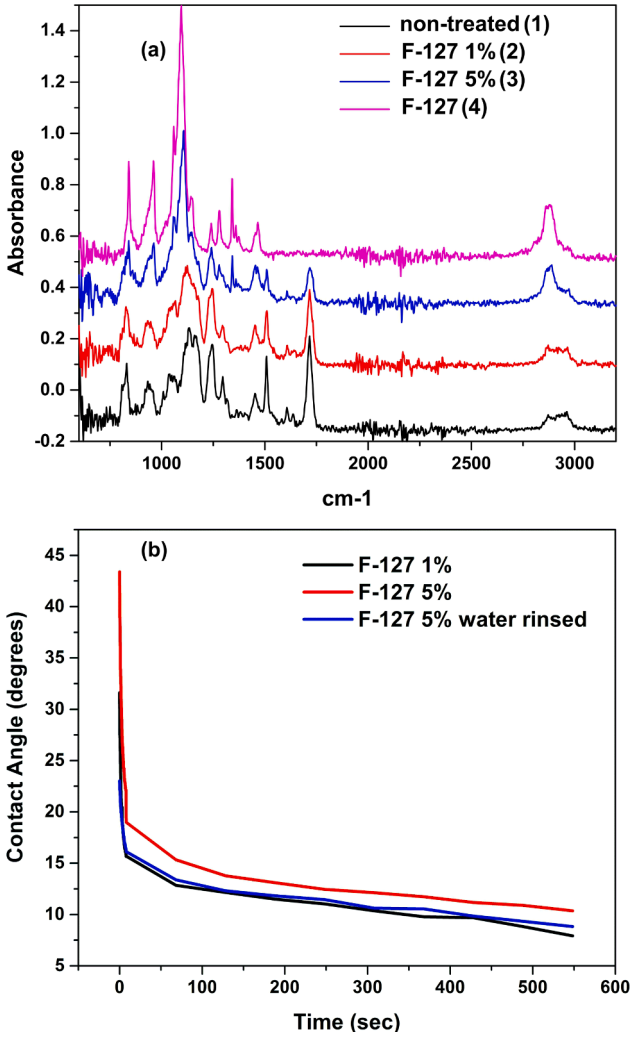

Fig. 5. (a) FTIR spectroscopy of 3D-printed resin films. (b) Contact angle goniometry studies of 3D-printed resin films coated with F-127 Pluronic solutions.

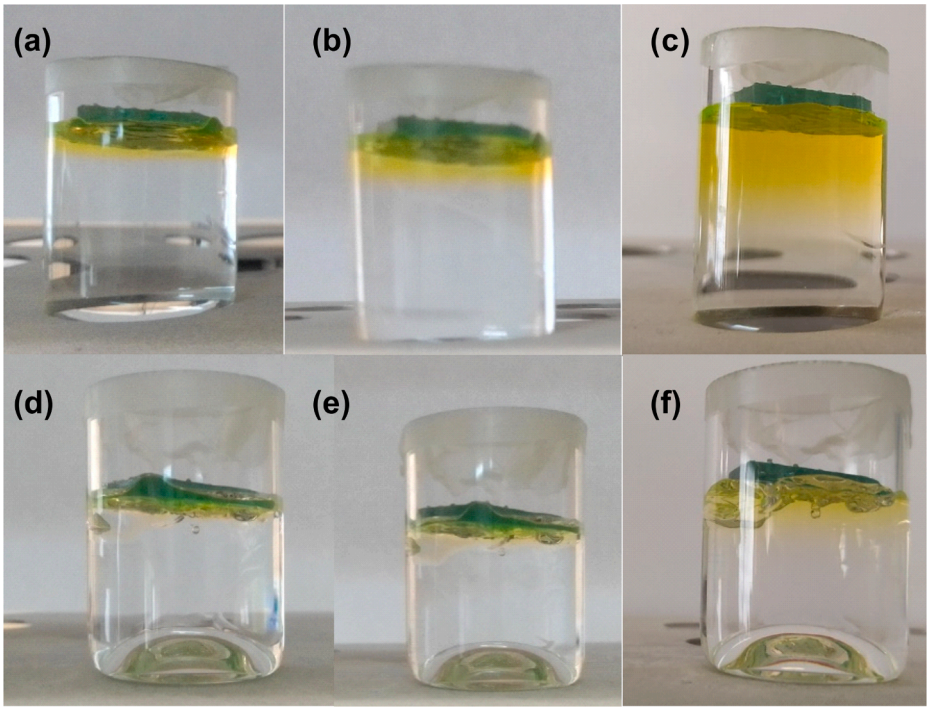

Fig. 6. Calcein diffusion at (a) 1 h, (b) 3 h and (c) 24 h. FITC-Dextran diffusion at (d) 1 h, (e) 3 h and (f) 24 h.

configuration exceeded the height of 1000 μm (Fig. 4(d)) increasing the possibility of painful perforation of the skin layers. By removing an arced part of the triangular-pyramid HMNs, the curved configuration resulted as shown in Fig. 4(a). In every case, tip area was no>0.00365 mm^2, while the minimum tip value was reduced down to 41.9 μm, as shown in Fig. 4(c).

Thereby, the previous analyses showed that the optimal printing angle was −52.63°. In addition, the average height of HMNs was measured to be 900 ± 40 μm, with a tip diameter of 51.9 ± 10 μm. The average projected area of the hole formations was found to be 0.222 ± 0.016 mm^2 and tip area 0.00340 ± 0.00025 mm^2. HMNs were designed in CAD with a height of 1000–1250 μm and a triangular tip area of 0.00125 mm^2. The microneedles' hole projected area was designed to be 0.2826 mm^2, interspacing was set at 3000 μm (center to center distance) and the whole patch was a 15 × 15 mm square. The optimal curing time was set at 70 s for the first 12 layers and at 10 s for the rest of them. The first layers, also referred as burn-in layers, were cured in 70 s since it was important for the base of the printlet to be properly attached to the printing platform. Different curing time 5 s and 15 s were examined as well. However, 5 s proved to be inadequate for effective polymerization whereas 15 s increased printing time allowing polymerization of excess resin material and leading to clogging of HMN channels and tip radius increase. Layer thickness at 30 μm provided the necessary repeatability level. The supports were manually generated ensuring they are located at a safe distance from any critical features (microneedles and their hole formation).

3.2. Microfluidic characterization

The mass flow capability was assessed using either isopropyl alcohol or aqueous solutions of methylene blue. Isopropyl alcohol solutions were easily pumped through the HMN channels and stained the filter paper whereas aqueous solutions of the dye were striving to flow into them. The latter might be attributed to the high surface tension between the aqueous medium and polymerized resin. The hydrophobic surface of the HMN channels was converted to hydrophilic by coating with Pluronic F-127 a non-ionic biocompatible surfactant. Upon surfactant's addition, aqueous solutions of methylene blue were effortlessly flowing through the HMN channels and filter paper was immediately stained.

To further demonstrate that no blockages occurred inside microneedle channels, HMN patches were cut using microtome so that HMNs are middle cross sectioned. Optical photographs were taken from the lateral view of HMNs and HMN channels were imaged. This visual material is presented in Fig. 3(f), (g). As seen, channels were narrowed from bottom to top which might be attributed to flow resin effect, but no clogs were captured.

FTIR spectroscopy and contact angle measurements were employed to elucidate the underlying mechanisms (Ferreira et al., 2020; Zhao et al., 2013). Fig. 5(a) depicts FTIR spectra of the 3D printed films i) without coating, ii) films coated with 1% w/v Pluronic F-127 solution, iii) films coated with 5% w/v Pluronic F-127 solution and iv) the pure surfactant. Results showed that upon coating little or no changes were observed among the treated films [compare spectra i) and ii)]. However, upon increasing the surfactant concentration from 1% to 5% w/v, film-treated spectra resemble similarities with the spectrum of Pluronic F-127 which might be attributed to efficient coating of the surface. Further quantification was attempted by monitoring spectral changes of esteric carbonyl group peak which is centered at 1700 cm^{-1} peak (spectrum of non-treated resin) and obtained due to esteric monomers. This peak was absent when looking at surfactant's spectrum. Upon treatment of the resin with different concentrations of surfactant, a decrease to the intensity of esteric carbonyl peak is observed. The percentage coverage (PC) attributed to any changes of the carbonyl intensity is given by the following equation:

$$PC = \frac{peak\ area\ of\ curve\ (non\ treated) - peak\ area\ of\ curve\ (treated)}{peak\ area\ of\ spectrum\ (non\ treated)} \times 100$$

The PC values for spectra ii) and ii) were 25% and 62% when treated with 1% w/v Pluronic F-127 solution and 5% w/v Pluronic F-127 solution accordingly. The latter implies an increase of the hydrophilic character of the surface which in turn facilitate a smooth passage of the formulation through the channels.

The findings obtained with FTIR were further corroborated by

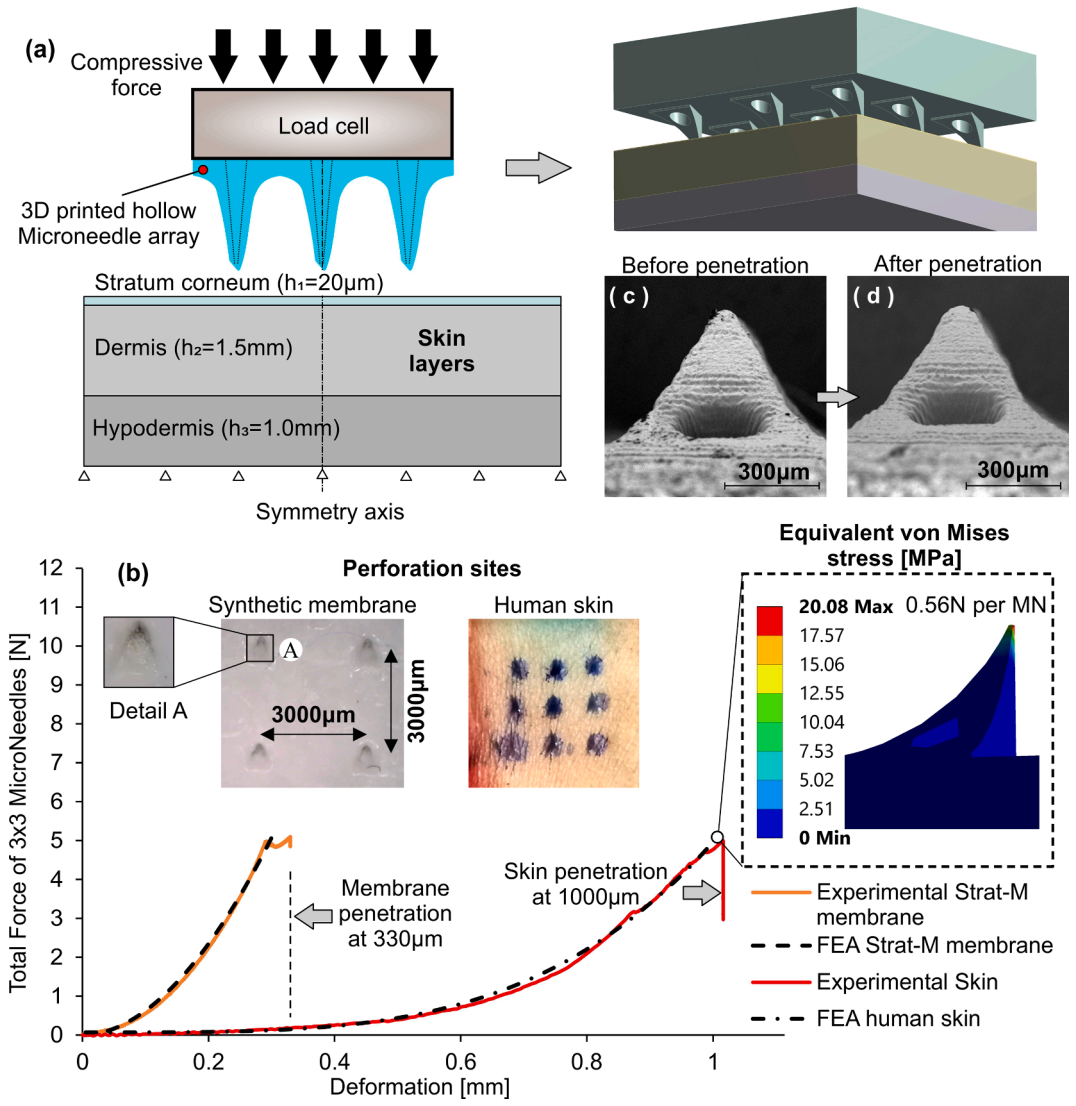

Fig. 7. Penetration tests using the optimized curved HMNs: (a) schematic representation of FEA simulation, (b) insertion force–deformation curve-fitted by FEA along with the perforation sites for both skin and skin-like synthetic membrane, (c) SEM of a microneedle before penetration testing and after penetration testing (indicating that there is not observed any tip failure).

contact angle measurements. The results showed that the presence of the surfactant reduced the water-substrate contact angle significantly. The contact angle of the non-coated 3D printed film (control) was $65.8 \pm 0.7^{\circ}$, which was constant over time. Treatment with Pluronic F-127 solution increased water wetting and dynamic effects were observed. The contact angle rapidly dropped to $15 \pm 2^{\circ}$ in all 3D printed films in<10 s. After this time the contact angle decreased at a slow rate reaching values below 10° (Fig. 5(b)). The rapid decrease of contact angle during the first seconds of wetting manifests the ability of the material to act as a substrate. Measurements were taken from different points of the material and they did not present contact angle variations higher than 1.5°, indicating the homogeneous performance of the material. Consequently, the differences observed in Fig. 5(b) upon treatment with 1% and 5% surfactant solution are considered insignificant. It is also notable that water rinsed 3D printed films (5% Pluronic coating) presented identical behavior compared to their non-rinsed congeners implying that upon dosage administration pluronic coating remains intact on film surface.

Finally, the diffusion of two model dyes, namely calcein (M.W.622.5 Da) and FITC Dextran (M.W. 4000 Da) upon application of the HMNs onto polyacrylamide gels was assessed. Photos were taken at 1 h, 3 h and 24 h (Fig. 6) demonstrating that HMNs were able to transfer model dyes of different molecular weight enabling their diffusion into the gels. The extent of the observed diffusion depends strongly on molecular weight when compare the upper panel of images (calcein) with the lower panel (FITC-Dextran) (Fig. 6(a)–(f)).

3.3. Mechanical behavior and penetration tests

Penetration tests were performed with human skin and synthetic Strat-M® membranes. The later are equivalent to all three layers of human skin. The tight top layer is representative of SC. The thickness of each Strat-M® membrane is approximately 300 μm and comprises of a top layer supported by two layers of porous polyether sulfone (PES). All previous layers are located on the top of one single layer of polyolefin non-woven fabric support (Haq et al., 2018b). In an attempt to evaluate the ultimate strength of the 3D-printed HMNs, failure tests were conducted on three separate HMN arrays (3 × 3). These compression tests were conducted using a force magnitude up to 400 N. Prior and after penetration and compression testing, any changes to HMNs were captured with an optical microscope and electron microscopy.

In order to advance the calculation accuracy of the skin and membrane penetration tests, a FEA simulation was performed. An explicit dynamics FEA based on the ANSYS code was utilized to investigate the

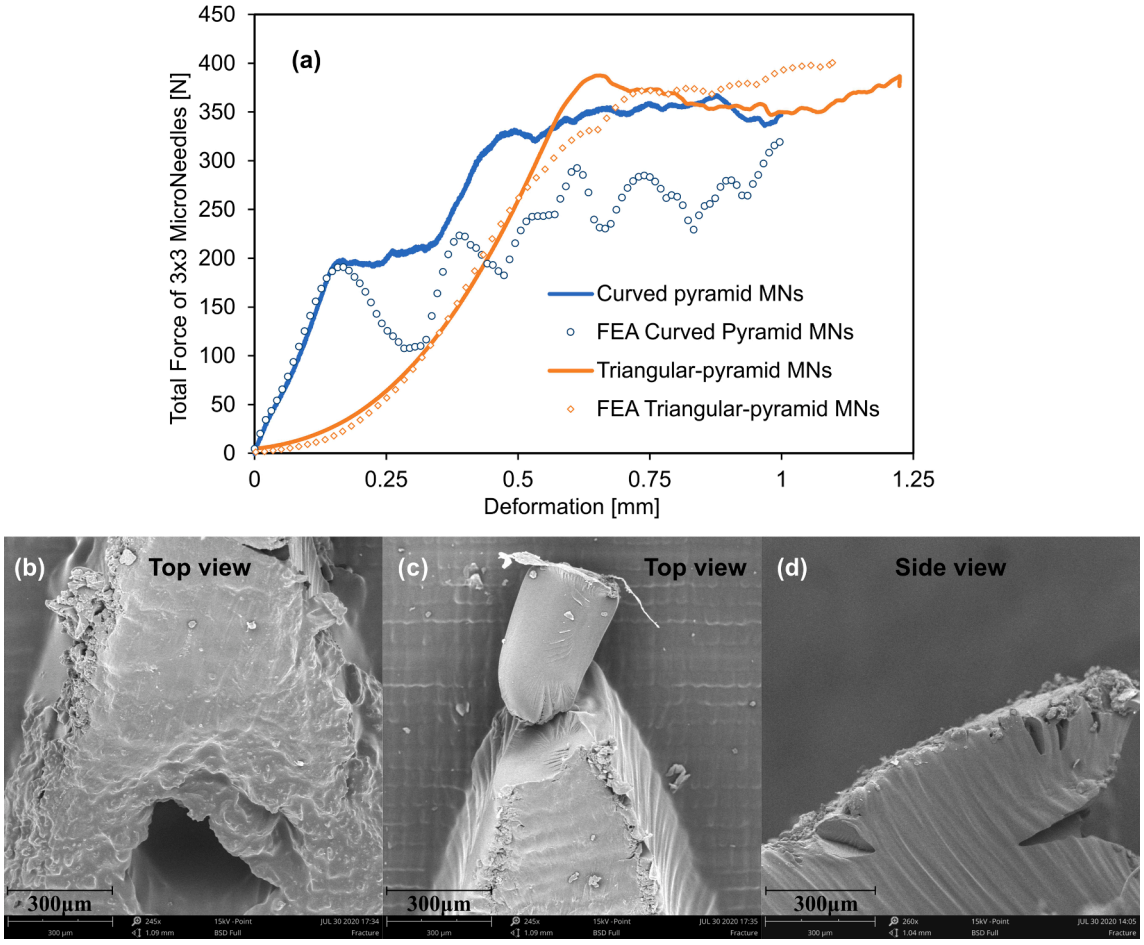

Fig. 8. Failure tests (a) Ultimate strength experimental data compared to the FEA simulation results, (b), (c), (d) HMN deformation after compression test.

insertion process of 3D printed HMN arrays into human skin. A multi-layered skin model consisting of three layers, SC, dermis and hypodermis, previously demonstrated was considered suitable (Xenikakis et al., 2019). This study showed that the skin deformation during the insertion process, as well as the insertion force of the microneedle for perforating the skin surface, agreed with the experimental data. In the current study, the experimental load-penetration depth data converged with the employed FEA model simulating the insertion of 3x3 HMNs into human skin and the synthetic membranes. By utilizing compression and nano-indentation mechanical testing techniques (Mansour et al., 2019, 2018; Tzetzis et al., 2017) the compressive strength of the NextDent 3D-printed resin material was determined to be 135 ± 5 MPa and the elastic modulus 1400 MPa.

In Fig. 7(a), a representation of the FEA model is illustrated, where the HMN arrays, the boundary conditions and the three layers of the skin are clearly presented. These three layers are equivalent to the main skin layers. More specifically, the first layer represents SC and has been given a thickness of $h_1 = 20$ μm, the second layer is equivalent to the dermis where $h_2 = 1.5$ mm and the third layer to the hypodermis where $h_3 = 1.0$ mm. Material failure and an evolving contact surface between HMNs and target was introduced, in order to define the insertion of the HMN array and the surface of the membrane samples, which is governed by large deformations. A material erosion algorithm was utilized to study the failure and separation of the material. The material erosion method removes distorted elements during the solution, i.e. along the HMN trajectory, based upon material failure and separation due to fracturing of the surface of the membrane and the skin. Since the hypodermis layer is not involved with failure and significant deformation, the first two layers, SC and dermis, were modeled as hyperelastic and elastic material, respectively.

The initial values of the mechanical properties of the SC, the dermis and the hypodermis assumed in these simulations were acquired by previous work and literature (Tran et al., 2007; Xenikakis et al., 2019). The material parameters were defined by fitting the FEA force-depth with the experimental data. Thus, the identification procedure could be considered as a minimization problem. A Neo-Hookean material model was considered very efficient in a previous work (Xenikakis et al., 2019), so its model parameters (C_{10}, K) were explored in order to minimize the difference between the computationally-generated force–displacement curves and the experimental penetration test data. Therefore, the skin properties for SC were determined as $C_{10} = 0.15$ MPa, $K_{SC} = 5.2$ MPa, for dermis: $C_{10} = 1.0$ MPa, $K_D = 25$ MPa and an elastic behavior was considered for the equivalent hypodermis layer with Poisson's ratio of 0.48 and Young's modulus of 3.2×10^4 Pa. The synthetic membrane properties were relatively similar to those of skin; SC: $C_{10} = 0.17$ MPa, $K_{SC} = 5.3$ MPa, for dermis: $C_{10} = 1.1$ MPa, $K_D = 30$ MPa and the equivalent hypodermis layer converged with a Poisson's ratio of 0.48 and a Young's modulus of 4.3×10^4 Pa. The insertion speed of the hollow microneedle array into the synthetic membrane and skin layers was set constant at 0.5 mm/min. The HMNs used in the simulation were the optimized curved HMNs with a triangular tip diameter 50 μm and length 900 μm.

Penetration tests revealed that perforation for both the human skin and Strat-M® membrane did occur at 5 N. The penetrated membrane and skin are shown in Fig. 7(b). Methylene blue staining confirmed perforation of SC. The bottom left spot of Fig. 7(b) misses blue dot at the perforation site, and this can be explained by skin inconsistencies and method limitations (Kochhar et al., 2013). This magnitude of 5 N force

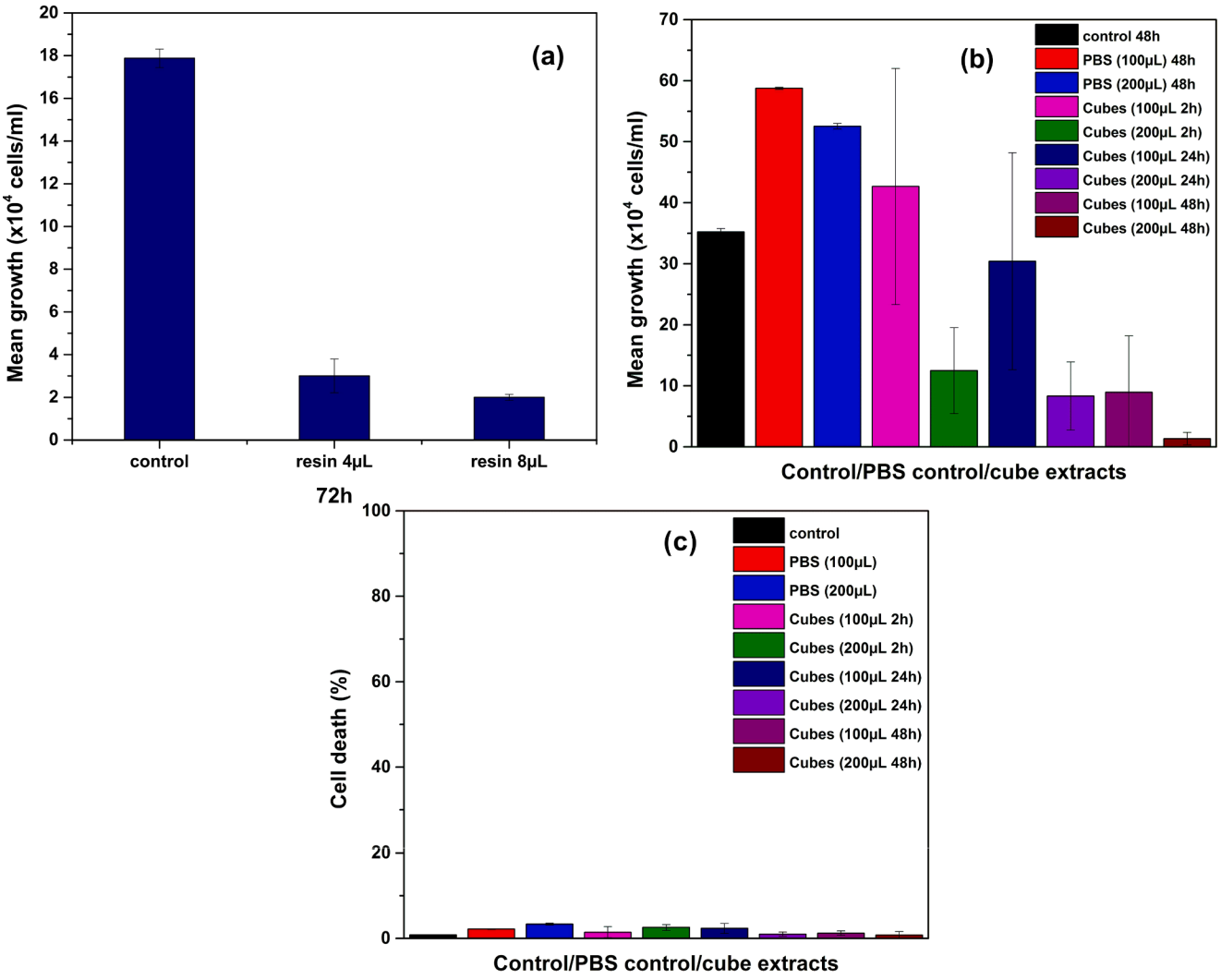

Fig. 9. Influence of resin (a) and cubic extracts (b) on cell growth. (c) Influence of cube extracts on cell death (n = 3 ± S.D.)

corresponds to a gentle push on human skin and is considered to be well tolerated from individuals (Kundu et al., 2018). A force–displacement curve is illustrated in Fig. 7(b). The general behavior of the HMN force–displacement history was obtained by the numerical simulation. Fig. 7(b) shown that the simulations were reasonably accurate and in a good agreement with the experimental load-depth curve for a maximum force of 5 N. In this load-depth curve during the deformation phase the force steadily increases, as each HMN is forced against the skin and synthetic membrane. Since the assumptions of the FEA converged to the experimental data, the optimal hyperelastic and elastic material model parameters were determined for the skin and the synthetic membrane.

It can be concluded that mechanical behavior of the three equivalent layers of the synthetic membrane was similar to skin. The insertion force for puncturing SC was calculated by FEA at 5.06 N, i.e. 5.06/9 = 0.56 N per microneedle, while for the first layer of the synthetic membrane the model converged at 5.12 N, i.e. 5.12/9 = 0.57 N per HMN. According to this correlation of penetration test supported by FEA, these synthetic membranes have potential to be used as an alternative to human skin. In terms of the actual process, while the HMN array descends, the skin and the equivalent layers of the membrane retract at the contact area and tends to curve around the HMN tips. The simulation of the penetration test revealed that the stress concentration was located at the tip of the HMNs, as displayed by the equivalent von Mises stress results in Fig. 7 (b). This demonstrates the stress contouring of the FEA simulating the behavior of the HMN at the last step of the penetration test simulation. The main concern was the concentration of the acquired stress at the tip region of the HMN. The maximum stress experienced by the insertion process was calculated to be 20.08 MPa, while the ultimate compressive strength was measured 135 ± 5 MPa, as mentioned previously. SEM images of the microneedles pre- and post- skin penetration testing are displayed in Fig. 7(c) and (d). These SEM images validate the results of the simulation and verify that the HMN tips did not exceed the compressive strength to induce any rupture phenomena, nor exhibited any visible residual deformation and local buckling after penetration.

Following penetration tests, a uniaxial compression load was applied directly onto the HMN array. Mechanical failure tests were conducted and simulated utilizing the triangular-pyramid and curved HMN arrays, in order to identify the force distribution and the position of maximum force, which corresponds to HMN's crucial point of failure. As shown in Fig. 8(a), yielding was observed at 380 ± 20 N for the triangular pyramid HMN array. The proposed optimized curved HMNs revealed a yield force of 190 ± 7 N and an ultimate force at 367 ± 8 N. Therefore, both configurations of HMNs revealed a fracture force around 400 N. Compression failure tests of the optimized curved HMNs in Fig. 8(a) reveal that yield strength was 21 N/microneedle and failure strength was 42 N/HMN. These values are significantly above the 0.56 N/HMN insertion force, thus validating the proposed curved HMN suitability for on-body applications.

After applying an axial load of 190 N, the optimized curved HMNs were compressed and lost about 15% of their height. Resin material at

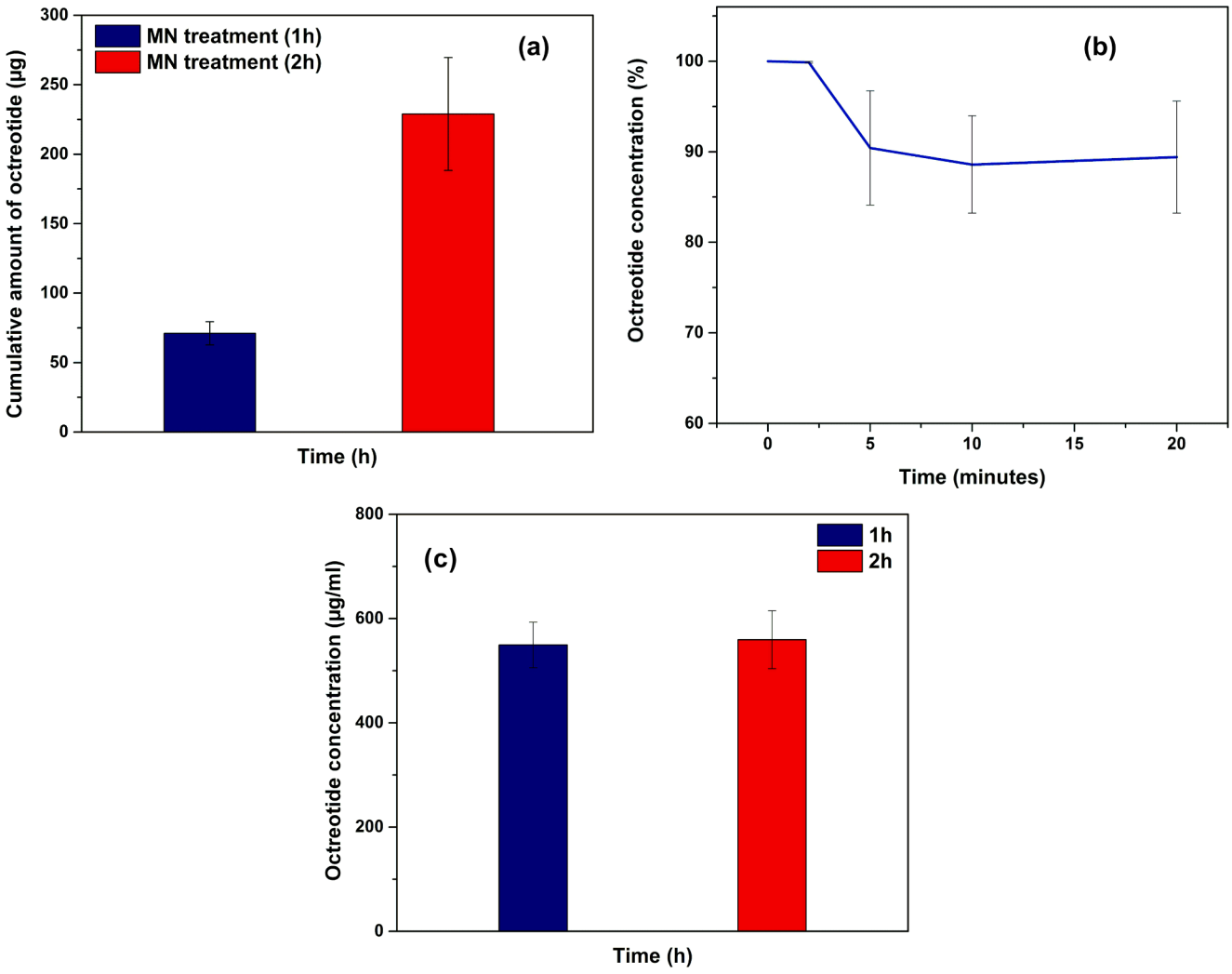

Fig. 10. (a) Permeation studies across synthetic membranes (n = 3 ± S.D.), (b) Binding studies of octreotide acetate and HMNs coated with Pluronic F-127 solution (n = 2) and (c) Stability of octreotide -acetate at 37 °C (n = 2).

the tip area was forced to fracture, as shown in Fig. 8(b). This material often obstructed fully or partially the microchannels. The tips resulted to a blunter shape whereas in some cases parts from the tips were detached, but not fully separated from the rest HMN corpus (Fig. 8(c)). Thus, complete facture was difficult to be achieved. The most common observation of this analysis was the compression of solidified resin and color alteration. Due to compression and after force removal, sharp cuts were also observed on various areas of the HMNs (Fig. 8(d)).

Summarizing the mechanical test results, puncturing of skin and synthetic membrane occurred with an insertion force of 5 N. Considering this experimental force as the puncturing force and dividing it with the number of HMNs (3x3) in the array, it can be easily calculated that the load being applied at each HMN separately is 0.56 N.

The insertion force values reported in the current study are in good agreement with a similar study (Yeung et al., 2019). Yet, it should be highlighted that force per HMN varies according to the number of HMNs are being included in an array alongside with their special geometric and material characteristics. Moreover, it is worth mentioning that the insertion force is particularly lower than the forces determined by compression failure testing of the HMNs thereby no fracture is anticipated. Regarding the Safety factor (SF) which is defined as the $F_{fracture}/F_{insertion}$ in the current study this ratio was found equal to 73.46. For $SF > 1$, safe application of HMNs is guaranteed because no fracture occurs during insertion which further indicate that the fabricated HMNs can be safely applied with no fragments remaining in tissues after retraction. Therefore, it can be concluded that the aforementioned HMN arrays could be safely used for skin penetration from a mechanical perspective.

3.4. Cytocompatibility assessment

The cytocompatibility of the commercial resin NextDent Ortho Rigid was evaluated in HaCaT cells. The presence of resin (4 μL and 8 μL respectively) caused a significant reduction (*t*-test, $p > 0.05$) to cell growth up to 83.21% and 88.81% respectively compared to control (Fig. 9(a)). This might be attributed to the fact that resins contain hazardous components such as photo-initiators and monomers easily converted to free radicals. Resin induced cell detachment which in turn caused cell death. The result obtained upon incubation of the extracts with the cells are presented in Fig. 9(b). Both PBS controls exert inductive action on cells, as cell growth is enhanced compared with the positive control. An increased inhibition to the cell growth was recorded for both volumes of extracts tested (100 and 200 μL). However, the phenomenon was more pronounced when 200 μL were co-incubated with the cells whereas all tested cube were not cytotoxic as evidenced in Fig. 9(c) with cell death percentage close to controls (not significant different, *t*-test, $p < 0.05$).

Summarizing cytocompatibility studies showed that cube PBS extracts may cause inhibition of cell growth, however cell death was not observed in the cultures. This observation, in combination with the fact

that HMN devices are designed for a few minutes' administration, the small skin area exposed to the device during administration (smaller than cubes' surface), the post fabrication treatment which includes both alcohol rinsing and ultrasonic bath for monomer removal and the SF which is > 1, renders the fabricated devices safe for drug administration.

3.5. Diffusion studies

Permeation studies were conducted using Strat-M® membranes as the best surrogate of human skin compared to other cellulose acetate or polymer membranes (Haq et al., 2018b, 2018a; Kaur et al., 2018). The transport of Octreotide acetate across synthetic membranes is shown in Fig. 10(a). As evidenced from the graph the amount of octreotide acetate was increased as a function of time reaching almost the half of the initial amount.

The interactions between the surface of the HMNs and the peptide are shown in Fig. 10(b). During the first two min drug retention is negligible (<0.25%) following by a drop up to 9.5% for the next 5 min and reaching the maximum binding 11.5% at 10 min advocating interactions between the hydrophilic chains of the surfactant and the peptide.

Proteins are prone to structural alterations even with slight variation of the keeping conditions. (Marczak et al., 2016). Stability studies at 37 °C revealed that octreotide is stable at the timescale of 2 h (Fig. 10 (c)).

4. Conclusions

In the current study HMNs were fabricated combining NextDent Ortho Rigid biocompatible resin and LCD method. Triangular-pyramid HMNs with printing angle of −52.63° were established as the most promising geometry for permeation studies. The wettability of the HMNs channels was significantly improved upon coating with a surfactant as evidenced from FTIR spectroscopy and contact angle measurements whereas gel diffusion experiments with dyes of low and high molecular weight drugs demonstrated the suitability of HMNs for drug transport. Prior to permeation studies, mechanical tests showed that fracture was observed after applying much higher forces compared to those of skin penetration process. The insertion force from penetration tests and SF calculation show that the fabricated HMN device will not fracture during skin application. FEA simulation of penetration and failure tests were in accordance with experimental findings. Preliminary toxicological assessment of HMN device showed that the main constituent of the microneedles, the resin, cause inhibition of cell growth, however HMNs were not cytotoxic. Finally, *in vitro* permeation studies revealed that HMN appears to be a feasible approach for peptide delivery.

CRediT authorship contribution statement

Iakovos Xenikakis: Data curation, Formal analysis, Investigation, Methodology, Project administration, Software, Validation, Visualization, Writing - original draft, Writing - review & editing. **Konstantinos Tsongas:** Data curation, Formal analysis, Investigation, Methodology, Project administration, Software, Validation, Visualization, Writing - original draft, Writing - review & editing. **Emmanouil K. Tzimtzimis:** Data curation, Formal analysis, Investigation, Methodology, Software, Validation, Visualization. **Constantinos K. Zacharis:** Data curation, Formal analysis, Investigation, Methodology, Validation, Visualization. **Nikoleta Theodoroula:** Data curation, Formal analysis, Investigation, Methodology, Validation, Visualization. **Eleni P. Kalogianni:** Data curation, Investigation, Methodology, Validation. **Euterpi Demiri:** Methodology, Validation, Visualization. **Ioannis S. Vizirianakis:** Methodology, Supervision, Validation, Visualization. **Dimitrios Tzetzis:** Conceptualization, Formal analysis, Methodology, Project administration, Resources, Software, Supervision, Validation, Visualization, Writing - review & editing. **Dimitrios G. Fatouros:** Conceptualization, Formal analysis, Funding acquisition, Methodology, Project administration, Resources, Software, Supervision, Validation, Visualization, Writing - review & editing.

Declaration of Competing Interest

The authors declare that they have no known competing financial interests or personal relationships that could have appeared to influence the work reported in this paper.

References

Calatayud-Pascual, M., Sebastian-Morelló, M., Balaguer-Fernández, C., Delgado-Charro, M., López-Castellano, A., Merino, V., 2018. Influence of Chemical Enhancers and Iontophoresis on the In Vitro Transdermal Permeation of Propranolol: Evaluation by Dermatopharmacokinetics. Pharmaceutics 10, 265.

Davis, S.P., Martanto, W., Allen, M.G., Prausnitz, M.R., 2005. Hollow Metal Microneedles for Insulin Delivery to Diabetic Rats. IEEE Trans. Biomed. Eng. 52, 909–915.

Doraiswamy, A., Jin, C., Narayan, R.J., Mageswaran, P., Mente, P., Modi, R., Auyeung, R., Chrisey, D.B., Ovsianikov, A., Chichkov, B., 2006. Two photon induced polymerization of organic-inorganic hybrid biomaterials for microstructured medical devices. Acta Biomater. 2, 267–275.

Farias, C., Lyman, R., Hemingway, C., Chau, H., Mahacek, A., Bouzos, E., Mobed-Miremadi, M., 2018. Three-Dimensional (3D) Printed Microneedles for Microencapsulated Cell Extrusion. Bioengineering 5, 59.

Ferreira, I.C.C., Aguiar, E.M.G., Silva, A.T.F., Santos, L.L.D., Cardoso-Sousa, L., Araújo, T. G., Santos, D.W., Goulart, L.R., Sabino-Silva, R., Maia, Y.C.P., Li, C.J., 2020. Attenuated Total Reflection-Fourier Transform Infrared (ATR-FTIR) Spectroscopy Analysis of Saliva for Breast Cancer Diagnosis. J. Oncol. 2020, 4343590.

Gallo, R.L., 2017. Human Skin Is the Largest Epithelial Surface for Interaction with Microbes. J. Invest. Dermatol. 137, 1213–1214.

Gieseke, M., Senz, V., Vehse, M., Fiedler, S., Irsig, R., Hustedt, M., Sternberg, K., Nölke, C., Kaierle, S., Wesling, V., Tiggesbäumker, J., Meiwes-Broer, K.H., Seitz, H., Schmitz, K.P., Haferkamp, H., 2012. Additive manufacturing of drug delivery systems. Biomed. Tech. 57, 398–401.

Gittard, S.D., Miller, P.R., Boehm, R.D., Ovsianikov, A., Chichkov, B.N., Heiser, J., Gordon, J., Monteiro-Riviere, N.A., Narayan, R.J., 2011. Multiphoton microscopy of transdermal quantum dot delivery using two photon polymerization-fabricated polymer microneedles. Faraday Discuss. 149, 171–185.

Gittard, S.D., Ovsianikov, A., Chichkov, B.N., Doraiswamy, A., Narayan, R.J., 2010. Two-photon polymerization of microneedles for transdermal drug delivery. Expert Opin. Drug Deliv. 7, 513–533.

Gomes-Porras, M., Cárdenas-Salas, J., Álvarez-Escolá, C., 2020. Somatostatin analogs in clinical practice: A review. Int. J. Mol. Sci. 21, 1682.

Gupta, J., Felner, E.I., Prausnitz, M.R., 2009. Minimally Invasive Insulin Delivery in Subjects with Type 1 Diabetes Using Hollow Microneedles. Diabetes Technol. Ther. 11, 329–337.

Guy, R.H., 1996. Current status and future prospects of transdermal drug delivery. Pharm. Res. 13, 1765–1769.

Haq, A., Dorrani, M., Goodyear, B., Joshi, V., Michniak-Kohn, B., 2018a. Membrane properties for permeability testing: Skin versus synthetic membranes. Int. J. Pharm. 539, 58–64.

Haq, A., Goodyear, B., Ameen, D., Joshi, V., Michniak-Kohn, B., 2018b. Strat-M® synthetic membrane: Permeability comparison to human cadaver skin. Int. J. Pharm. 547, 432–437.

Ingrole, R.S.J., Gill, H.S., 2019. Microneedle coating methods: A review with a perspective. J. Pharmacol. Exp. Ther. 370, 555–569.

Jamroz, W., Kurek, M., Lyszczarz, E., Brniak, W., Jachowicz, R., 2017. Printing techniques: recent developments in pharmaceutical technology. Acta Pol. Pharm. 74, 753–763.

Karpiński, T.M., 2018. Selected medicines used in iontophoresis. Pharmaceutics 10, 204.

Kaur, L., Singh, K., Paul, S., Singh, Sukhprit, Singh, Shashank, Jain, S.K., 2018. A Mechanistic Study to Determine the Structural Similarities Between Artificial Membrane Strat-M™ and Biological Membranes and Its Application to Carry Out Skin Permeation Study of Amphotericin B Nanoformulations. AAPS PharmSciTech 19, 1606–1624.

Kim, Y.-C., Park, J.-H., Prausnitz, M.R., 2012. Microneedles for drug and vaccine delivery. Adv. Drug Deliv. Rev. 64, 1547–1568.

Kochhar, J.S., Goh, W.J., Chan, S.Y., Kang, L., 2013. A simple method of microneedle array fabrication for transdermal drug delivery. Drug Dev. Ind. Pharm. 39, 299–309.

Kundu, A., Ausaf, T., Rajaraman, S., 2018. 3D printing, ink casting and micromachined lamination (3D PICLμM): A makerspace approach to the fabrication of biological microdevices. Micromachines 9.

Larrañeta, E., McCrudden, M.T.C., Courtenay, A.J., Donnelly, R.F., 2016. Microneedles: A New Frontier in Nanomedicine Delivery. Pharm. Res. 33, 1055–1073.

Lau, D.T.W., Sharkey, J.W., Petryk, L., Mancuso, F.A., Yu, Z., Tse, F.L.S., 1994. Effect of Current Magnitude and Drug Concentration on Iontophoretic Delivery of Octreotide Acetate (Sandostatin®) in the Rabbit. Pharm. Res. 11, 1742–1746.

Luttge, R., Berenschot, E.J.W., de Boer, M.J., Altpeter, D.M., Vrouwe, E.X., van den Berg, A., Elwenspoek, M., 2007. Integrated Lithographic Molding for Microneedle-Based Devices. J. Microelectromechanical Syst. 16, 872–884.

Ma, B., Liu, S., Gan, Z., Liu, G., Cai, X., Zhang, H., Yang, Z., 2006. A PZT insulin pump integrated with a silicon microneedle array for transdermal drug delivery. Microfluid. Nanofluidics 2, 417–423.
Mansour, M., Tsongas, K., Tzetzis, D., 2019. Measurement of the mechanical and dynamic properties of 3D printed polylactic acid reinforced with graphene. Polym. Technol. Mater. 58, 1234–1244.
Mansour, M., Tsongas, K., Tzetzis, D., Antoniadis, A., 2018. Mechanical and Dynamic Behavior of Fused Filament Fabrication 3D Printed Polyethylene Terephthalate Glycol Reinforced with Carbon Fibers. Polym. Plast. Technol. Eng. 57, 1715–1725.
Marczak, M., Okoniewska, K., Grabowski, T., 2016. Classification model of amino acid sequences prone to aggregation of therapeutic proteins. Silico Pharmacol. 4.
Martanto, W., Moore, J.S., Kashlan, O., Kamath, R., Wang, P.M., O'Neal, J.M., Prausnitz, M.R., 2006. Microinfusion using hollow microneedles. Pharm. Res. 23, 104–113.
Miller, P.R., Gittard, S.D., Edwards, T.L., Lopez, D.A.M., Xiao, X., Wheeler, D.R., Monteiro-Riviere, N.A., Brozik, S.M., Polsky, R., Narayan, R.J., 2011. Integrated carbon fiber electrodes within hollow polymer microneedles for transdermal electrochemical sensing. Biomicrofluidics 5, 13415.
Mohamed, M.G.A., Kumar, H., Wang, Z., Martin, N., Mills, B., Kim, K., 2019. Rapid and inexpensive fabrication of multi-depth microfluidic device using high-resolution LCD stereolithographic 3D printing. J. Manuf. Mater. Process 3.
Moussi, K., Bukhamsin, A., Hidalgo, T., Kosel, J., 2020. Biocompatible 3D Printed Microneedles for Transdermal, Intradermal, and Percutaneous Applications. Adv. Eng. Mater. 22, 1901358.
Nguyen, H.X., Banga, A.K., 2018. Electrically and Ultrasonically Enhanced Transdermal Delivery of Methotrexate. Pharmaceutics 10 (3), 117.
Olatunji, O., Das, D.B., Garland, M.J., Belaid, L., Donnelly, R.F., 2013. Influence of Array Interspacing on the Force Required for Successful Microneedle Skin Penetration: Theoretical and Practical Approaches. J. Pharm. Sci. 102, 1209–1221.
Ovsianikov, A., Chichkov, B., Mente, P., Monteiro-Riviere, N.A., Doraiswamy, A., Narayan, R.J., 2007. Two Photon Polymerization of Polymer?Ceramic Hybrid Materials for Transdermal Drug Delivery. Int. J. Appl. Ceram. Technol. 4, 22–29.
Pérennès, F., Marmiroli, B., Matteucci, M., Tormen, M., Vaccari, L., Fabrizio, E. Di, 2006. Sharp beveled tip hollow microneedle arrays fabricated by LIGA and 3D soft lithography with polyvinyl alcohol. J. Micromech. Microeng. 16, 473–479.
Prausnitz, M.R., 2017. Engineering Microneedle Patches for Vaccination and Drug Delivery to Skin. Annu. Rev. Chem. Biomol. Eng. 8, 177–200.
Roxhed, N., Gasser, T.C., Griss, P., Holzapfel, G.A., Stemme, Gö, 2007. Penetration-Enhanced Ultrasharp Microneedles and Prediction on Skin Interaction for Efficient Transdermal Drug Delivery. J. Microelectromechanical Syst. 16, 1429–1440.
Schramm-Baxter, J., Katrencik, J., Mitragotri, S., 2004. Jet injection into polyacrylamide gels: Investigation of jet injection mechanics. J. Biomech. 37, 1181–1188.
Touitou, E., 2002. Drug delivery across the skin. Expert Opin. Biol. Ther. 2, 723–733.
Tran, H. V., Charleux, F., Rachik, M., Ehrlacher, A., Ho Ba Tho, M.C., 2007. In vivo characterization of the mechanical properties of human skin derived from MRI and indentation techniques. Comput. Methods Biomech. Biomed. Engin. 10, 401–407.
Tzetzis, D., Tsongas, K., Mansour, G., 2017. Determination of the mechanical properties of epoxy silica nanocomposites through FEA-supported evaluation of ball indentation test results. Mater. Res. 20, 1571–1578.
van der Maaden, K., Heuts, J., Camps, M., Pontier, M., Terwisscha van Scheltinga, A., Jiskoot, W., Ossendorp, F., Bouwstra, J., 2018. Hollow microneedle-mediated micro-injections of a liposomal HPV E743–63 synthetic long peptide vaccine for efficient induction of cytotoxic and T-helper responses. J. Control. Release 269, 347–354.
van der Maaden, K., Sekerdag, E., Jiskoot, W., Bouwstra, J., 2014. Impact-insertion applicator improves reliability of skin penetration by solid microneedle arrays. AAPS J. 16, 681–684.
Waghule, T., Singhvi, G., Dubey, S.K., Pandey, M.M., Gupta, G., Singh, M., Dua, K., 2019. Microneedles: A smart approach and increasing potential for transdermal drug delivery system. Biomed. Pharmacother. 109, 1249–1258.
Xenikakis, I., Tzimtzimis, M., Tsongas, K., Andreadis, D., Demiri, E., Tzetzis, D., Fatouros, D.G., 2019. Fabrication and finite element analysis of stereolithographic 3D printed microneedles for transdermal delivery of model dyes across human skin in vitro. Eur. J. Pharm. Sci. 137, 104976.
Yeung, C., Chen, S., King, B., Lin, H., King, K., Akhtar, F., Diaz, G., Wang, B., Zhu, J., Sun, W., Khademhosseini, A., Emaminejad, S., 2019. A 3D-printed microfluidic-enabled hollow microneedle architecture for transdermal drug delivery. Biomicrofluidics 13 (6), 064125.
Zhao, Y.-Z., Lv, H.-F., Lu, C.-T., Chen, L.-J., Lin, M., Zhang, M., Jiang, X., Shen, X.-T., Jin, R.-R., Cai, J., Tian, X.-Q., Wong, H.L., 2013. Evaluation of a Novel Thermosensitive Heparin-Poloxamer Hydrogel for Improving Vascular Anastomosis Quality and Safety in a Rabbit Model. PLoS One 8, 73178.